Clonal Dynamics of Cancer-Initiating Cells in a Mouse Genetic Mosaic Model of Serous Ovarian Cancer

Jianhao Zeng[a], Eli Casarez[a], Ying Jiang[a], Astrid Catalina Alvarez-Yela[b], Lixin Wang[b], Brianna E. Kelly[a], Eugene Ke[a], Taylor Jenkins[c], Kristen A. Atkins[c,d], Kevin A. Janes[b,d], Jill K. Slack-Davis[a,d*], Hui Zong[a,d*].

[a] Department of Microbiology, Immunology, and Cancer Biology, [b] Department of Biomedical Engineering, [c] Department of Pathology, and [d] Cancer Center, University of Virginia, Charlottesville, Virginia, United States of America.

* Corresponding author. hz9s@virginia.edu (Hui Zong) jks6a@virginia.edu (Jill K. Slack-Davis)

Classification

Biological Science; Medical Sciences.

Keywords

Ovarian Cancer, Fallopian Tube, Cancer Initiation, Premalignant Clonal Dynamics, Genetic Mosaic Mouse Model

Author Contributions

- J.Z., J.K.SD., and H.Z. designed research.
- J.Z., E.C., Y.J., L.W., and B.E.K. performed research.
- J.Z., A.C.AY., E.K., T.J., K.A.A, K.A.J, and H.Z. analyzed data.
- J.Z., A.C.AY., K.A.J, J.K.SD., and H.Z. wrote the paper.

This PDF file includes:

Main Text

Figures 1-5

Figures S1-7

HIGHLIGHTS

- Ovarian cancer initiation revealed by a mouse genetic mosaic model.
- Dichotomous expansion capacity of initiated cells at the clonal level.
- Synergies between cell-intrinsic properties and onco-mutations fuels clonal expansion.
- Imbalanced differentiation within highly expansive clones leads to Pax8 clusters.

ABSTRACT

High-grade serous ovarian cancer (HGSOC) is the most lethal gynecologic malignancy. Early detection remains the most promising strategy to decrease mortality and requires a deep understanding of the cancer initiation process. Recent breakthroughs identified the fallopian tube (FT) Pax8+ cells as a cell-of-origin for HGSOC. However, the progressive trajectory from an initiated Pax8+ cell toward malignancy remains elusive. Here, we use a mouse genetic mosaic system called MADM (Mosaic Analysis with Double Markers), which generates sporadic mutant cells labeled with GFP, to trace the clonal dynamics of HGSOC development. Surprisingly, we observed dichotomous clonal expansion kinetics of individual cancer-initiating Pax8+ cells; while the vast majority stalled immediately, a few significantly expanded. Clonal analysis of wildtype cells showed concordant dichotomy, suggesting that a small fraction of Pax8+ cells intrinsically carry higher expansion potential. Furthermore, although all wildtype clones stalled shortly after development, some mutant clones continued to progress, indicating that oncogenic mutations prolong clonal expansion beyond the cell-intrinsic potential. Finally, intra-clonal fate mapping revealed that progressing mutant clones have a higher propensity to produce Pax8+ cells, linking imbalanced cell differentiation to disease progression. In summary, our studies reveal that the earliest clonal expansion during HGSOC initiation emerges when oncogenic mutations exaggerate the intrinsic expansion potential of a rare Pax8+ subset and bias its differentiation potential, warranting future investigation as a readout for early detection and cancer prevention.

SIGNIFICANCE STATEMENT

Effective early detection is the most promising approach to manage cancer, but it requires a thorough understanding of cancer initiation and early progression. Serous ovarian cancer has been found to originate from Pax8+ cells in the fallopian tube. To assess the clonal dynamics of cancer-initiating cells, we established a mouse genetic mosaic model that enables clonal analysis of mutant Pax8+ cells in the fallopian tube. We uncovered that the earliest clonal event in ovarian cancer development emerges from a rare subset of stem/progenitor-like cells with intrinsic expansion potential, and that oncogenic mutations exaggerate and prolong this potential to promote cancer initiation. Our findings pinpoint a precise target for future early-detection and cancer prevention studies.

INTRODUCTION

Cancer is the second leading cause of death in the United States. Early detection and intervention remain the most promising approach for successful management of cancer (1, 2). For instance, the introduction of Pap smear testing reduced cervical cancer mortality by 50% (3), and modern mammography screening reduced breast cancer mortality by 28% (4). However, effective early detection is not readily available for every cancer type, such as ovarian cancer, which has a <30% 5-year survival rate when diagnosed at malignant stages (5). Although screening with serum CA125 achieved earlier detection of ovarian cancer by 10%, it didn't significantly improve the 5-year survival rate (6, 7). More effective early detection is urgently needed, and it requires a thorough understanding of the natural history of cancer, including the identification the cancer cell-of-origin and the tracking of its evolution prior to malignancy.

High-grade serous ovarian cancer (HGSOC) is the most prevalent and aggressive ovarian cancer subtype and causes about 14,000 deaths annually in the United States (8, 9). While malignant tumors arise in the ovary, recent clinical studies and mouse-modeling pinpointed the fallopian tube (FT) as the origin for a large portion of HGSOCs (10-17). The FT is a long tubal channel that connects the ovary and uterus and consists of ciliated cells (Acetyl-Tubulin+) that facilitate gamete transportation and secretory cells (Pax8+) that produce nutrient-rich fluid (18). The Pax8+ cell has been implicated as the cancer cell-of-origin, because human FT precursor lesions are predominantly comprised of Pax8+ cells, and introducing relevant oncogenic mutations into FT Pax8+ cells in transgenic mice led to HGSOC (10, 16). However, the progressive trajectory from an initiated Pax8+ cell toward malignancy remains elusive. Understanding how clinically relevant oncogenic mutations alter the cellular behavior of FT Pax8+ cells to initiate carcinogenesis and whether all Pax8+ cells, which account for >50% of FT epithelium, are equally able to initiate cancer upon genetic mutation should provide critical insights for HGSOC early detection.

Mouse models have played powerful roles in cancer research, including providing concrete evidence that support Pax8+ cells as a cell of origin for HGSOC. However, most conventional mouse models are not suitable for studying cancer initiation, because they tend to create too many mutant cells, the behavior of which cannot be studied until they manifest pathological features (19). To overcome this hurdle, our lab has developed a mouse genetic system called Mosaic Analysis with Double Markers (MADM) that concomitantly generates a GFP+ mutant cell and its RFP+ wildtype sibling cell from a non-labeled heterozygous mother cell through Cre/loxP-mediated inter-chromosomal mitotic recombination (**Fig. 1*A***) (20, 21). The rarity of mutant cells attributed to the low frequency of inter-chromosomal recombination (0.1%–1% or even lower) closely mimics the clonal origin of human cancer, and the immediate and unequivocal GFP-labeling of mutant cells enables clonal analysis right at cancer initiation (20, 22, 23). Taking advantage of the unprecedented temporal and spatial resolution of MADM, here we assess clonal expansion kinetics of initiated FT Pax8+ cells to uncover the earliest steps of HGSOC development.

RESULTS

Establishment of a MADM-based mouse model to study premalignant progression of mutated FT Pax8+ cells at clonal resolution.

To establish a MADM-based model for HGSOC initiation, two critical prerequisites need to be considered: 1) HGSOC-relevant tumor suppressor genes that reside on the telomeric side of the MADM cassettes; 2) a Cre transgene that is known to target the cell-of-origin for HGSOC. Based on TCGA data, we found that the loss of *TP53* (63%), *BRCA1/2* (78%) and the mutations that activate the Ras-MAPK pathway (37%, partially through loss of *NF1*) are among the most prevalent genetic alterations and often co-occur in human HGSOC patients (**Fig. S1*A***) (24-28). Since *TP53, BRCA1,* and *NF1* all reside on mouse chromosome-11 where the MADM cassettes had been knocked-in (**Fig. S1*B*)** (29), we selected these mutations to drive tumor initiation. To target the cancer cell-of-origin in a controlled manner, we incorporated the Pax8-rtTA; TetO-Cre system (16, 30, 31). After breeding the mutations and the Cre system into two MADM stock lines (**Fig. S1*C*** and see methods for details), we established MADM-mutant mice to model HGSOC initiation and early progression in the FT (**Fig. 1*B***). This breeding scheme also generates MADM-wildtype mice as a control (**Fig. S1*C***).

To assess the frequency and faithfulness of labeling in this MADM model, we induced Cre activity in MADM-wildtype mice between postnatal day 1 and 21 (P0-21) with doxycycline (DOX) in the drinking water and found that ~0.2% of FT epithelial cells (FTEs) were GFP+ or tdTomato+, a sparsity that allows clonal tracing over time (**Fig. 1*C*, *D***). Yellow cells were found at ~8-fold higher rate due to G2-Z segregation during mitosis or G0/G1 recombination (**Fig. 1*D*, S2*A*, *B***). We confirmed the faithfulness of the Cre system by checking the Pax8 status of labeled cells in FTs after a short-term (P19-21) Cre induction; nearly all MADM-labeled cells were positive for Pax8 (**Fig. 1*E*, *F***). Thus, the MADM-based mouse generates sparse, GFP-labeled mutant cells in the FT Pax8+ population to model cancer initiation in the FT.

Quantitative clonal analysis reveals divergent expansion of individual initiated Pax8+ cells.

We next evaluated clonal expansion of individual mutant cells by inducing Cre activity between birth and weaning then analyzing FTs at five months (**Fig. 2*A***), a time when initiated cells have expanded but not yet formed histopathologically detectable lesions. To gain a full view of all clones, we optically cleared the FTs with the CUBIC method (32), imaged the entire FT with light-sheet microscopy, and quantified the size of each clone by reconstructing image stacks (**Fig. 2*B***). Interestingly, clone sizes were highly divergent (**Fig. 2*C***): ~75% of the clones contained < 10 cells, yet a small fraction of clones expanded to hundreds of cells or more (**Fig. 2*D***). To exclude the possibility that the dichotomy resulted from stochastic fluctuations, we implemented a mathematical analysis that evaluates whether the observed clonal size distribution can be explained by one single stochastic group. We estimated the clonal size distribution from the majority clones and asked whether the frequency of observed outlier large clones is within that predicted by the majority distribution. The observed clonal sizes were best fit by a negative binomial model for clones below 50 cells (KS test, p-value<0.1, see methods for details) (33). Under the null hypothesis, this one-group model predicts one clone larger than 50 cells. In contrast, we observed 27 clones larger than 50 cells, suggesting the existence of an outlier group (**Fig. 2*E***) ($p < 10^{-8}$, Fisher Exact Test) that has a higher expansion potential than most clones.

To determine when these outlier clones become detectable, we repeated the clonal size measurements with mice at one and two months of age (**Fig. 2*A***). To our surprise, profoundly expanded clones already existed among tiny ones shortly after Cre induction (**Fig. 2*F, G***). We ruled out the trivial explanation that this clonal size divergence simply reflects their differential birth-date over the 21-day period of DOX administration (P0-21) by demonstrating prominent clonal size variance even when clonal birth-date was limited within a 3-day time window (**Fig. S3**). Finally, we compared the frequency of outlier large clones from 1, 2, and 5 months of age.

Because the variance of clonal sizes at younger ages was smaller overall, a Poisson model was used to calculate the portion of outlier large clones (see methods for details). We found that the portion of outlier large clones at one month is 16.5 ± 4.4%, which increased to 28.4 ± 1.9% at two months and held steady at 30.9 ± 0.9% at five months (**Fig. 2*H***), suggesting that the expansion potential of initiated Pax8+ cells was determined at an early time point. Collectively, these data show that initiated FT Pax8+ cells present dichotomous expansion potential with the majority stalled and a small fraction profoundly expanded.

Spatial and molecular characterizations of expanded clones hint at a stem/progenitor-like origin.

The near-immediate divergence of clonal-expansion prompted us to ask whether the initial oncogenic mutations were absolutely required or if there was intrinsic heterogeneity of the expansion potential of Pax8+ cells. To address this question, we induced clones in the MADM-wildtype mice, in which clones of all colors are free of oncogenic mutations (**Fig. S1*C***). We examined the size of these wildtype clones at 1, 2, and 5 months of age and still observed evident clonal size divergence as early as 1 month of age (**Fig. 3*A, B***), indicating that the divergent clonal-expansion potential of Pax8+ cells could be intrinsic.

The high clonogenicity of some Pax8+ cells is reminiscent of stem/progenitor-like cells (34). Although definitive FT stem/progenitor cell markers are still lacking, several studies showed that these cells are within the Pax8+ subpopulation and are spatially enriched in the fimbrial (distal) portion of FTs (35-39). To assess whether the expanded clones show similar spatial preference as the FT stem/progenitor cells do, we stretched the FTs from MADM-wildtype mice and performed whole-mount imaging to examine the location of expanded clones. The FT comprises three different portions: the distal portion (D) consists of the fimbria and ampulla; the middle portion (M) consists of the isthmus; and the proximal portion (P) consists of the utero-tubal junction. Each portion can be discriminated by their distance to the ovary and

their unique ductal morphology (**Fig. 3*C*)**. When we examined clonal distribution in FTs of MADM-wildtype mice, we found that expanded clones reside almost exclusively in the distal FTs close to the ovary (**Fig. 3*D, E***). Similar spatial preference of expanded clones was also observed in FTs of MADM-mutant mice (**Fig. S4*A, B***). Such spatial preference was not caused by biased generation of more clones in the distal FT, because the initial labeling frequency by MADM was similar throughout FT segments (**Fig. S4*C***). Finally, we investigated whether the distal enrichment of highly cologenic cells was maintained in adult FT by inducing MADM labeling between 5-6 weeks age when the FT epithelium is considered fully developed (40). Examining clones one month after labeling again revealed a spatial enrichment of the expanded clones in the distal FT (**Fig. S4*D***), supporting a consistent predisposition to expand regardless of age or genotype.

Although definitive markers for FT stem/progenitor cells remain elusive, Rose et al. found an Aldh+ subpopulation enriched for stem/progenitor-like cells (38), and Dinh et al. have identified a progenitor-like subset with high expression of Thy1, Igfbp5, and Lgals1 (41). Moreover, Wnt and Notch pathways are reported to maintain FT stemness (35, 38, 42). To compare these candidate markers and pathways between small and expanded clones, we isolated them separately from MADM-wildtype mice using fluorescence-guided laser capture microdissection **(Fig. *3F*,** see methods for details**)**. We used FTs from mice that were one month old, when large clones are readily distinguishable from small clones by size but not so expanded that stem/progenitor signatures would be diluted beyond detection by ongoing differentiation. Using qRT-PCR, we compared the abundance of stem/progenitor-like cell markers (*Aldh1a1*, *Thy1*, *Igfbp5,* and *Lgals1*), Wnt pathway genes (*Ctnnb1*, *Wnt7b*, *Wnt16*, *Tcf7,* and *Lef1*) and Notch pathway genes (*Notch1*, *Notch2,* and *Olfm4*), and found that the large clones showed significantly higher expression of *Aldh1a1* and *Notch2* **(Fig. *3G*).** Taken together, the distal enrichment and unique molecular signatures of expanded clones hint at their stem/progenitor-origin.

Oncomutations synergize with cell-intrinsic potential for prolonged expansion of mutant clones.

To address how oncogenic mutations impact cancer initiation, we compared the proliferative rate between expanded wildtype and expanded mutant clones (corresponding to the outlier large clones) over time (**Fig. 4*A***). Measured by a 7-day EdU labeling immediately before harvest, expanded wildtype clones showed high proliferative rate at 1 month, which then dropped to very low at 2 and 5 months. (**Fig. 4*B*, *D, E***), suggesting that the initial expansion capacity subsides quickly by the end of FT development (39). While the proliferative rate of expanded mutant clones followed a similar trend over time, we noted two important differences. First, the decrease in overall proliferation at 2 and 5 months in mutant clones was not as dramatic as in wildtype ones (**Fig. 4*C, D, E***), suggesting that oncogenic mutations were able to sustain cell proliferation after the developmental window. Second, the proliferative rate of expanded mutant clones at 2 and 5 months of age showed a large variance, with some clones nearly as active as 1-month and others almost completed stopped (**Fig. 4*C, D, E,* Fig*. S*5**), suggesting that some expanded mutant clones sustained proliferative rate after development while others stopped. Consequently, some mutant clones became significantly larger at older ages even though their average size was comparable to wildtype clones at one month (**Fig. 4*F***), confirming a role for oncogenic mutations in prolonging proliferation in expanded mutant clones albeit not at full penetrance.

The long-term progressive mutant clones showed increased propensity to differentiate toward Pax8 fate, and fuel STICs formation.

The epithelium of the normal distal FT consists of interspersed Pax8+ cells (30%) and ciliated cells (70%) (**Fig. S6*A, B***) (43). On the contrary, precursor lesions in human FT such as "secretory-cell-outgrowths" (SCOUTs) and serous tubal intraepithelial carcinomas (STICs)

predominantly consist of uninterrupted stretch of Pax8+ cells (39, 44). We asked whether the expanded mutant clones, as a candidate intermediate between normal and disease, could reflect this cell composition shift towards more Pax8+ cells. Indeed, we observed uninterrupted stretches of Pax8+ cells in expanded mutant clones reminiscent of early-stage abnormalities in human, which contrasted the interspersed Pax8+ and Pax8- cells in the adjacent non-mutant regions (**Fig. 5*A***). As a result, the proportion of Pax8+ cells in the progressive mutant clones was significantly higher than adjacent non-mutant regions (**Fig. 5*B***). We hypothesized that the uninterrupted stretches of Pax8+ cells result from a biased propensity of proliferating mutant cells to differentiate toward Pax8+ fate. To test this hypothesis, we performed an EdU pulse-chase experiment to determine the fate of newly born cells within progressive clones (**Fig. 5*C***). First, we mapped the length of EdU pulse, and found that 3-day administration led to clonal labeling of proliferating cells (**Fig. S6*C-G***). Then we quantified EdU+ clonal sizes after 4-day chase and found that, while most wildtype clones remained at 1-2 cells, many mutant clones grew much larger (**Fig. S6*H-J***). When we examined the fate of cells in these EdU+ subclones, we found that, while 70% of cells in wildtype subclones had cilia, mutant EdU+ subclones were much less frequently ciliated (**Fig.5*D, E***), suggesting a high propensity of mutant cells to adopt a Pax8+ cell fate.

We then asked whether eventually these progressive mutant clones were capable of forming FT lesions, such as STICs. We examined H&E-stained FT sections from a total of 83 mice across a spectrum of ages and identified 6 GFP+ STICs among 40 mice aged 8-14 months (**Fig. 5*F, G***), suggesting that the expanded mutant clones are indeed capable of progressing further to STICs. The rarity of STICs was expected in the MADM system, because 1) in contrast to conditional knockout models, MADM only generates very few mutant cells initially; 2) among the initial mutant cells, only a small portion are capable of expanding (**Fig. 2**); 3) among the initially expanded clones, less than half of them maintain long-term proliferation (**Fig. 4*D, E***); and 4) we suspect that not every proliferative clone can eventually progress to

STIC. Aging of MADM mutant animals much beyond 1 year to assess the onset of full-blown HGSOC was not possible because mice succumbed to invasive tumors in the uterus, which also contains Pax8+ cells with transforming potential (45) (**Fig. S2*C***). Nevertheless, our results indicate that expanded mutant clones are capable for further progression and recapitulate early abnormalities observed in human HGSOC.

DISCUSSION

In this study, we established a mouse genetic mosaic system to model HGSOC initiation. Taking advantage of the single-cell resolution afforded by the model, we delineated the clonal dynamics of individual cancer-initiating cells. We found that while the majority of clones stall, a small number of clones sustain their expansion as a result of synergy between cell-intrinsic potential and oncogenic mutations. Specifically, we showed that regardless of genotype or age, large clones tend to be enriched at the distal FT, hinting at their stem/progenitor-origin; however, only clones with oncogenic mutations sustained long-term progression, whereas wildtype ones quickly became quiescent. Finally, intraclonal fate-mapping of proliferative cells in the progressive mutant clones revealed their imbalanced differentiation toward a Pax8+ fate, which matches well with clinical observations of HGSOC precursor lesions in the FT.

MADM as a tool to delineate clonal expansion dynamics of cancer-initiating cells.

Although delineating early clonal events during cancer initiation could shed light on effective early detection and prevention strategies, it remained underexplored due to the lack of patient samples prior to the development of pathologically identifiable lesions and a shortage of mouse models that allow the study of premalignant progression. To overcome this hurdle, we developed the MADM-based mouse model, which can generate rare, GFP-labeled mutant cells. This model not only provides access to the premalignant stages of cancer, but also allows us to study progression of individual initiated cells at the clonal level (22). In principle, this approach to model cancer initiation and premalignancy can be applied to any other cancer type and present a powerful tool to dissect the dynamics and heterogeneity of cancer initiating cells at the clonal resolution. The analytic power of the MADM-based model is further enhanced by an internal control, i.e., RFP-labeled wildtype sibling clones, and by MADM-wildtype control mice, which are critically useful for dissecting the intersection between onco-mutations and cell-

intrinsic properties during cancer initiation (46). When combined with EdU pulse-chase fate-mapping, one could further trace the behavior of actively proliferating cells within progressing mutant clones, providing a real-time assessment of the distribution pattern and fate of cells that fuel clone growth and progression (47).

The synergy between cell-intrinsic potential and oncogenic mutations underpins the long-term clonal progression from initiated Pax8+ cells towards FT precursor lesions.

The inherent properties of the cancer cell-of-origin provide a permissive context for oncogenes to initiate cancer (48-50). Within the FT, the Pax8+ cells have been identified as the cancer cell-of-origin for HGSOC (15, 16, 51, 52). However, whether all or only a subset of the Pax8+ cells could transform remains unknown. Through clonal tracing of sparsely generated mutant Pax8+ cells, we showed that only a small proportion of them undergo further progression. This group of cells harbor high expansion potential and elevated expression of putative FT stem/progenitor cell markers *Aldh1a1* and *Notch2* and are enriched in the distal FT, coinciding with reported location of FT stem cells (37, 53, 35, 36, 42). This set of data suggests that only stem/progenitor-like Pax8+ cells are predisposed to cancer initiation. Further characterization of these cells is warranted and could lead to the discovery of biomarkers for early detection.

How do oncogenic mutations alter the behavior of the cancer cell-of-origin? Through quantitative analysis of expansive Pax8+ clones with or without mutations over time, we found that the mutations not only enhance the extent of clonal expansion but also sustain their duration, resulting in evidently larger sized mutated clones. Besides cell proliferation, mutant cells in expanded clones also manifested biased differentiation toward a Pax8+ fate, resulting in bands of uninterrupted Pax8 cells, a feature often found in human precursor lesions known as SCOUTs and STICs (39). As the Pax8+ population contains FT stem/progenitor cells based on

previous lineage tracing studies (39), this biased cell fate may reflect a tendency to maintain stemness, a feature commonly found during the progression of many cancer types (54).

Implications of premalignant heterogeneity for cancer early-detection and prevention studies

Although the exact differences between the highly progressive and stalled Pax8+ cells need to be further explored, the clonal dynamics revealed by our study carries important implications for early detection and prevention studies of HGSOC. We uncovered a gradual attrition process of mutant Pax8+ cells during caner initiation and premalignant progression (**Fig. S7**). Initially, the vast majority of mutant cells stall while only a small portion expand. With time, among initially expanded clones, only some sustain their progressive expansion. Moreover, within continuously progressing mutant clones, only a small fraction of the cells maintain proliferative activity. This progression trajectory of initiated mutant cells indicates that one must focus solely on the rare proliferating cells within those continuously progressing mutant clones to discover early detection markers to guard against the risk for over-diagnosis. In another word, indiscriminative profiling of all mutant cells would bring in tremendous noise from stalled mutant cells and mask the true signal from progressive cells. For the same reason, to measure efficacy of cancer prevention strategies, one should sharply focus on those progressing cells rather than the bulk of mutant cells that already reached their dead end.

In summary, our study demonstrates the application of a mouse genetic mosaic system to dissect clonal dynamics of individual cancer initiating cells at an unprecedentedly early stage with single-cell resolution, which should pave the way for discovery of effective early detection markers and preventive strategies.

Materials and Methods

Animals

All animal procedures are approved by the Institutional Animal Care and Use Committee (IACUC) at the University of Virginia in accordance with national guidelines to ensure the humanity of all animal experiments. The following mouse lines were crossed to establish the MADM-mutant and MADM-wildtype mice: *TG11ML* (stock NO. 022976 JAX), *GT11ML* (stock NO. 022977 JAX), *BRCA1*^{flox} (strain NO. 01XC9 NCI), *NF1*^{flox} (strain no. 01XM4; NCI), *TP53*^{KO} (stock no. 002101; JAX), *PAX8-rtTA* (stock NO. 007176 JAX)(30), *TetO-Cre* (stock NO. 006234 JAX)(31).

In vivo drug delivery

Doxycycline was administered through the drinking water (2mg/ml) to the nursing mother, which transmit to MADM pups through milk (P0-P21) to induce Cre recombinase. 5-ethynyl-2'–deoxyuridine (27) (Invitrogen, Cat# A10044) was administered through drinking water (0.5mg/ml). EdU staining was performed following standard procedures (55).

Immunostaining

Reproductive tracts of MADM mice were harvested then fixed overnight with cold 4% paraformaldehyde (PFA) at 4°C. Tissues were then washed with PBS to remove recessive PFA, soaked with 30% sucrose, embedded in optimal cutting temperature (OCT), and stored at -80°C. The tissues were sectioned at 18μm thickness. For staining, slides were incubated in Permeabilization/blocking buffer (0.3% Triton-X 100 in PBS [PBT] plus 5% normal donkey serum) for 20 min then primary antibodies (Pax8,1:50,10336-1-AP, Proteintech; AcTUB,1:500, T7451, Sigma) diluted in Permeabilization/block buffer were added and incubated at 4°C overnight. Secondary antibody incubation was performed for 1 hour at RT in PBT. To stain nuclei, slides were incubated in DAPI solution (1ug/mL in PBT) for 5 min before mounting with 70% glycerol and covered. Fluorescent images were acquired on Zeiss LSM 700/710 confocal microscope. Images were processed with Zen and Fiji.

Tissue clearing with CUBIC method and 3D imaging

The PFA fixed ovary and fallopian tube were cleared for large-scale 3D imaging with the standard CUBIC method (32). Tissues were first immersed in 50% reagent-1 and shaken at 110 rpm, 37°C for 6h and then transferred to 100% reagent-1 with DAPI (1ug/ml) to shake for 2-3 days until becoming transparent. After reagent-1, tissues were washed three times with PBS, 30 mins each with shaking to remove the reagent-1. Tissues were immersed in 50% reagent-2 for 6h with shaking at 37°C; thereafter, buffer was exchanged to 100% reagent-2 with shaking for 24h.

The Zeiss Z.1 light-sheet microscopy system was used to acquire images. Tissues were embedded in 2% (w/w) agarose (LE quick dissolve agarose, GeneMate E-3119-500) gel; the agarose was dissolved in a modified reagent-2 (10% urea, 50% sucrose, 30% H_2O, hot stir at 80°C until fully dissolved, then add 10% Tri-ethanolamine). The warm agarose gel solution together with tissue was aspirated into a 1ml syringe with the neck cut off, and then the syringe was placed on ice for a quick solidification. The syringe was placed on the holder of the light-sheet microscope, and the tissue was pushed out for imaging.

Counting clone size

Whole FT were cleared and imaged at 5 um intervals with light-sheet microscopy at single-cell resolution through the entire tissue. Three-dimensional reconstruction of clones was performed; labeled cells that were found at the exact location through multiple image stacks were counted as one clone. The size of clones was measured manually by counting the DAPI-stained nuclei.

Mathematical detection of outlier clones.

The clonal size distribution along the fallopian tube was evaluated in terms of cell division events. With n as the number of cells per clone, there will be n-1 cell divisions. For clonal size distribution at five months, we fitted with a negative binomial distribution, which captures the behavior of the over-dispersed data observed in our mouse models, by allowing the mean and variance to be different. Clonal size distribution at 1 and 2 months, which showed a smaller

range, were fitted with a Poisson distribution. To estimate the statistical significance of our fitting, we generated null distributions for the Kolmogorov-Smirnov (KS) statistic between an ideal probability mass function and a random negative binomial/Poisson distribution over 1.000 iterations. The parameters used for generating the null distributions were obtained by merging all datasets and taking a maximum of 44/8-9-10, which showed significance in our first general screening. Then, the empirical nominal p-value of the observed KS for the merged data was calculated relative to the null distribution until a cutoff with significance was observed. Our final cutoff was set as the maximum number of divisions for which the probability of observing our KS was $p >= 0.1$. The validity of this cutoff was confirmed by evaluating the individual datasets over the null distributions. Then, the maximum expected clonal sizes (n) in the fallopian tube were calculated, and any clone with a size larger than n was taken as the outlier. Subsequently, we computed the expected clone sizes for all the models, and we tested their significance against the observed values in our datasets using Fisher exact/Chi-square tests. Finally, we defined over-proliferative clones (Expected - observed outliers) for the size distributions observed under the Poisson model and tested their significance between 1, 2, and 5 months by an Anova with Tukey's Honest Significant Difference test.

Fluorescence-guided laser-capture micro-dissection of fallopian tube epithelial cells

Cryo-embedded fresh FTs were sectioned at 8 μm thickness and were then dehydrated with 70% ethanol (30 sec), 95% ethanol (30 sec), and 100% ethanol for 1 min, followed by clearing with xylene (2 min). After air drying, slides were micro-dissected with Arcturus XT LCM instrument (Applied Biosystems) and Capsule HS caps (Arcturus). The typical instrument settings of ~50 mW power and ~2 ms duration with the smallest spot size were used.

RNA extraction, reverse transcription and amplification for quantitative PCR

The procedures were described before (56). In brief, RNA from the micro-dissected cells were extracted through enzymatic digestion with proteinase K (Sigma), then reverse transcribed with 5'-biotin modified oligo(dT)24 (IDT) and SuperScript III (50 °C, 30 min; then heat inactivation at

70 °C for 15 min). The first-strand products were purified with Streptavidin magnetic beads (Pierce) and Super Magnet Plate (Alpaqua) to remove genomic DNA. Then the cDNA was poly(A)-tailed and amplified with 25 cycles of PCR with AL1 primer:

ATTGGATCCAGGCCGCTCTGGACAAAATATGAATTCTTTTTTTTTTTTTTTTTTTTTTTTT

Real-time quantitative PCR

For detection of specific genes with the amplified samples, qPCR was performed with CFX96 real-time PCR instruments (Bio-Rad). One ul of amplified cDNA was diluted with 449 ul ddH_2O, then 4.5 µl were used as template for a 15 µl qPCR system. SYBR Green was used for detection. QPCR primers for each gene were selected based on three requirements: 1) 90-110% amplification efficiency, 2) single melting peak, and 3) single band of 100-200 bp on agarose gel. QPCR were run for 40 cycles followed by a default Melting Curve program. Each run was performed in duplicate; the expression levels were normalized to the geometric mean of three housekeeping genes.

The qPCR primers list:

Target Genes	Forward	Reverse
GAPDH	GGCATTGCTCTCAATGACAA	GCCTCTCTTGCTCAGTGTCC
EpCAM	TGGCACTGCTAACTGGTACAAA	GTCAGTGGCAGAGCAGATACA
Ck18	GGAGTCAGAGCTGGCACAAA	CAGGGCATCGTTGAGACTGA
Pax8	CCCTGGAAAGTTCAGTGAGGCT	TTGGGGGTCTCTTCAGTGGC
Ovgp1	TCCATTGGTGGCAAATCCGA	TGCCCCATAACGGTTTGTGA
Thy1	GACCTCCTAATCTCAGGGGC	ATACATGGTGATGGGACAGGC
Lgals1	TCAAGATTAAGTGCGTGGCCT	TCTCCCATGAAAGGGCTGGA
Aldh1a1	GCAAGCTCTCTGTAACTCCGT	TTTCACAACACCTGGGGAACA
Igfbp5	TCCTTCAGATTCCGAGACGC	GAGAGGACAGAGCTACGGTG
β-Catenin	TTTATCGGGGATACGTGCGG	CCGCATCTGTTGAAGCATTGT
Wnt7b	TGATGCCACCGAGGCAATTC	CCTGGGTCCACTAACCACCT
Wnt16	GTCGCTGCCTGTAAGAGTGT	TCCCAAATCATCCAAAGGCGA
Tcf7	GCATCTTGCACTTAGGATGGC	TGTTCCCAGGTGGAGAAACAC
Notch1	CGTGTGTCAAGCTGATGAGGA	CCATCCTGGGTTGTGCTCTTA
Notch2	AAGAAAGCCGTCAGCACGA	AGTCCGGGTCCTGAAATCAC
Olfm4	TCCTGGAATTTGCAAGAAAGTGA	AAAGCCACCAGAGGATCTGC

Acknowledgments

We thank Dr. Zhe Li, Xiaoyu Zhao and Bing Xu for providing critical feedback on the manuscript and Joceylyn Ray for the artwork of the fallopian tube cartoon. We also thank Dr. Stacey Criswell at the Advanced Microscopy Facility, Dr. Pat Pramoonjago at the Biorepository and Tissue Research Facility, Sheri Vanhoose at the Research Histology Core, and Shelly Verling at the vivarium for their assistance on the project. These core facilities are supported by UVA Cancer Center grant #P30-CA044579. We are grateful to Dr. Ammasi Periasamy and Dr. Ruofan Cao at the Keck Center for the usage of the Lightsheet Z.1 microscopy system. This work was partly supported by the Department of Defense Ovarian Cancer Research Program #W81XWH-17-1-0174 (J.K.S-D. & H.Z.), the Rivkin Center (H.Z.), the UVA Cancer Center Seed Grant (J.K.S-D. & H.Z.), and the UVA Cancer Center Training Grant (J.Z.).

References

1. Society. AC (2022.) Cancer Facts & Figures 2022. *Atlanta: American Cancer Society;* .
2. Siegel RL, Miller KD, Fuchs HE, & Jemal A (2022) Cancer statistics, 2022. *CA Cancer J Clin* 72(1):7-33.
3. Arbyn M*, et al.* (2010) European Guidelines for Quality Assurance in Cervical Cancer Screening. Second edition--summary document. *Ann Oncol* 21(3):448-458.
4. Weedon-Fekjaer H, Romundstad PR, & Vatten LJ (2014) Modern mammography screening and breast cancer mortality: population study. *BMJ* 348:g3701.
5. Seidman JD*, et al.* (2004) The histologic type and stage distribution of ovarian carcinomas of surface epithelial origin. *Int J Gynecol Pathol* 23(1):41-44.
6. Usha Menon AG-M, Matthew Burnell, Naveena Singh, Andy Ryan, Chloe Karpinskyj, Giulia Carlino, Julie Taylor,, Susan K Massingham MR, Jatinderpal K Kalsi, Robert Woolas, Ranjit Manchanda, Rupali Arora, Laura Casey, Anne Dawnay, Stephen Dobbs,, Simon Leeson TM, Mourad W Seif, Aarti Sharma, Karin Williamson, Yiling Liu, Lesley Fallowfield, Alistair J McGuire, Stuart Campbell,, & Steven J Skates IJJ, Mahesh Parmar (2021) Ovarian cancer population screening and mortality after long-term follow-up in the UK Collaborative Trial of Ovarian Cancer Screening (UKCTOCS): a randomised controlled trial. *The Lancet* 397(10290):P2182-2193.
7. Jacobs IJ*, et al.* (2016) Ovarian cancer screening and mortality in the UK Collaborative Trial of Ovarian Cancer Screening (UKCTOCS): a randomised controlled trial. *The Lancet* 387(10022):945-956.
8. Siegel RL, Miller KD, & Jemal A (2020) Cancer statistics, 2020. *CA Cancer J Clin* 70(1):7-30.
9. Vaughan S*, et al.* (2011) Rethinking ovarian cancer: recommendations for improving outcomes. *Nat Rev Cancer* 11(10):719-725.
10. Karnezis AN, Cho KR, Gilks CB, Pearce CL, & Huntsman DG (2017) The disparate origins of ovarian cancers: pathogenesis and prevention strategies. *Nat Rev Cancer* 17(1):65-74.
11. Keren Levanon CC, Ronny Drapkin (2008) New insights into the pathogenesis of serous ovarian cancer and its clinical impact. *J Clin Oncol* 26(32):5284-5293.
12. Fabiola Medeiros MGM, Yonghee Lee, Julia A Elvin, Michael J Callahan, Colleen Feltmate, Judy E Garber, Daniel W Cramer, Christopher P Crum (2006) The tubal fimbria is a preferred site for early adenocarcinoma in women with familial ovarian cancer syndrome。. *The American journal of surgical pathology* 30(2):230-236.
13. Press JZ*, et al.* (2008) Ovarian carcinomas with genetic and epigenetic BRCA1 loss have distinct molecular abnormalities. *BMC Cancer* 8:17.
14. Barakat RR FM, Saigo PE, Robson ME, Offit K, Boyd J. (2000) Absence of premalignant histologic, molecular, or cell biologic alterations in prophylactic oophorectomy specimens from BRCA1 heterozygotes. *Cancer* 89(2):383-390.
15. Lee Y*, et al.* (2007) A candidate precursor to serous carcinoma that originates in the distal fallopian tube. *J Pathol* 211(1):26-35.
16. Perets R*, et al.* (2013) Transformation of the fallopian tube secretory epithelium leads to high-grade serous ovarian cancer in Brca;Tp53;Pten models. *Cancer Cell* 24(6):751-765.
17. Labidi-Galy SI*, et al.* (2017) High grade serous ovarian carcinomas originate in the fallopian tube. *Nat Commun* 8(1):1093.
18. Stewart CA & Behringer RR (2012) Mouse Oviduct Development. *Mouse Development: From Oocyte to Stem Cells*, ed Kubiak JZ (Springer Berlin Heidelberg, Berlin, Heidelberg), pp 247-262.
19. Cheon DJ & Orsulic S (2011) Mouse models of cancer. *Annu Rev Pathol* 6:95-119.
20. Zong H, Espinosa JS, Su HH, Muzumdar MD, & Luo L (2005) Mosaic analysis with double markers in mice. *Cell* 121(3):479-492.

21. Mandar Deepak Muzumdar 1 LL, Hui Zong (2007) Modeling sporadic loss of heterozygosity in mice by using mosaic analysis with double markers (MADM). *Proc Nati Acad Sci USA* 104(11):4495-4500.
22. Liu C*, et al.* (2011) Mosaic analysis with double markers reveals tumor cell of origin in glioma. *Cell* 146(2):209-221.
23. Hippenmeyer S (2013) Dissection of gene function at clonal level using mosaic analysis with double markers. *Frontiers in Biology* 8(6):557-568.
24. Walsh T CS, Lee MK, Pennil CC, Nord AS, Thornton AM, Roeb W, Agnew KJ, Stray SM, Wickramanayake A, Norquist B, Pennington KP, Garcia RL, King MC, Swisher EM. (2011) Mutations in 12 genes for inherited ovarian, fallopian tube, and peritoneal carcinoma identified by massively parallel sequencing. *Proc Nati Acad Sci USA* 108(44):18032-18037.
25. Anonymous (2011) Integrated genomic analyses of ovarian carcinoma. *Nature* 474(7353):609-615.
26. Ahmed AA*, et al.* (2010) Driver mutations in TP53 are ubiquitous in high grade serous carcinoma of the ovary. *J Pathol* 221(1):49-56.
27. Patch AM*, et al.* (2015) Whole-genome characterization of chemoresistant ovarian cancer. *Nature* (1476-4687 (Electronic)).
28. Angela Toss CT, Elisabetta Razzaboni,Giannina Contu,Giovanni Grandi,Angelo Cagnacci,Russell J. Schilder,and Laura Cortesi. (2015) Hereditary Ovarian Cancer: Not Only BRCA 1 and 2 Genes. *Biomed Res Int* (341723).
29. Tasic B*, et al.* (2012) Extensions of MADM (mosaic analysis with double markers) in mice. *PLoS One* 7(3):e33332.
30. Traykova-Brauch M*, et al.* (2008) An efficient and versatile system for acute and chronic modulation of renal tubular function in transgenic mice. *Nat Med* 14(9):979-984.
31. Anne-Karina T Perl SEW, Andras Nagy, Corrinne G Lobe, Jeffrey A Whitsett (2002) Early restriction of peripheral and proximal cell lineages during formation of the lung. *PNAS* 99(16):10482-10487.
32. Susaki EA*, et al.* (2015) Advanced CUBIC protocols for whole-brain and whole-body clearing and imaging. *Nat Protoc* 10(11):1709-1727.
33. Fisher CIBaRA (June 1953) Fitting the Negative Binomial Distribution to Biological Data. *Biometric* 9(2):176-200.
34. Elaine Fuchs JAS (2000) Stem Cells. *Cell* 100(1):143-155.
35. Xie Y, Park ES, Xiang D, & Li Z (2018) Long-term organoid culture reveals enrichment of organoid-forming epithelial cells in the fimbrial portion of mouse fallopian tube. *Stem Cell Res* 32:51-60.
36. Daniel Y. Paik DMJ, Amanda M. Schafenacker, Victor S. Velasco, May S. Shung, Donghui Cheng, Jiaoti Huang, Owen N. Witte, and Sanaz Memarzadeh. (2012) Stem-like epithelial cells are concentrated in the distal end of the fallopian tube: a site for injury and serous cancer initiation. *Stem Cells* 30(11):2487–2497.
37. Wang Y*, et al.* (2012) Identification of quiescent, stem-like cells in the distal female reproductive tract. *PLoS One* 7(7):e40691.
38. Rose IM*, et al.* (2020) WNT and inflammatory signaling distinguish human Fallopian tube epithelial cell populations. *Sci Rep* 10(1):9837.
39. Ghosh A, Syed SM, & Tanwar PS (2017) In vivo genetic cell lineage tracing reveals that oviductal secretory cells self-renew and give rise to ciliated cells. *Development* 144(17):3031-3041.
40. Yamanouchi H, Umezu T, & Tomooka Y (2010) Reconstruction of oviduct and demonstration of epithelial fate determination in mice. *Biol Reprod* 82(3):528-533.

41. Dinh HQ*, et al.* (2021) Single-cell transcriptomics identifies gene expression networks driving differentiation and tumorigenesis in the human fallopian tube. *Cell Rep* 35(2):108978.
42. Mirjana Kessler KH, Volker Brinkmann, Oliver Thieck, Susan Jackisch, Benjamin Toelle, Hilmar Berger, Hans-Joachim Mollenkopf, Mandy Mangler, Jalid Sehouli, Christina Fotopoulou & Thomas F. Meyer. (2015) The Notch and Wnt pathways regulate stemness and differentiation in human fallopian tube organoids. *Nat Commun* 6(8989).
43. Harwalkar K*, et al.* (2021) Anatomical and cellular heterogeneity in the mouse oviduct-its potential roles in reproduction and preimplantation developmentdagger. *Biol Reprod* 104(6):1249-1261.
44. Chen EY*, et al.* (2010) Secretory cell outgrowth, PAX2 and serous carcinogenesis in the Fallopian tube. *J Pathol* 222(1):110-116.
45. David Tacha DZ, Liang Cheng. (2011) Expression of PAX8 in normal and neoplastic tissues: a comprehensive immunohistochemical study. *Appl Immunohistochem Mol Morphol* 19(4):293-299.
46. Phillippe P. Gonzalez JK, Rui Pedro Galvao,Nichola Cruickshanks,Roger Abounader,Hui Zong. (2018) p53 and NF 1 loss plays distinct but complementary roles in glioma initiation and progression. *Glia* 66(5):999-1015.
47. Driessens G, Beck B, Caauwe A, Simons BD, & Blanpain C (2012) Defining the mode of tumour growth by clonal analysis. *Nature* 488(7412):527-530.
48. Greaves M & Maley CC (2012) Clonal evolution in cancer. *Nature* 481(7381):306-313.
49. Lauren M.F. Merlo JWP, Brian J. Reid & Carlo C. Maley (2006) Cancer as an evolutionary and ecological process. *Nature Reviews Cancer* 6:924-935.
50. Visvader JE (2011) Cells of origin in cancer. *Nature* 469(7330):314-322.
51. Zhang S*, et al.* (2019) Both fallopian tube and ovarian surface epithelium are cells-of-origin for high-grade serous ovarian carcinoma. *Nat Commun* 10(1):5367.
52. Fabiola Medeiros MGM, Yonghee Lee, Julia A Elvin, Michael J Callahan, Colleen Feltmate, Judy E Garber, Daniel W Cramer, Christopher P Crum. (2006) The tubal fimbria is a preferred site for early adenocarcinoma in women with familial ovarian cancer syndrome. *The American journal of surgical pathology* 20(2):230-236.
53. Victoria Snegovskikh LM, Effi Massasa, and Hugh S. Taylor. (2014) Identification of Putative Fallopian Tube Stem Cells. *Reproductive Sciences*.
54. Alcolea MP*, et al.* (2014) Differentiation imbalance in single oesophageal progenitor cells causes clonal immortalization and field change. *Nat Cell Biol* 16(6):615-622.
55. Adrian (2008) A chemical method for fast and sensitive detection of DNA synthesis in vivo. *PNAS* 105(7):2415-2420.
56. Singh S*, et al.* (2019) In situ 10-cell RNA sequencing in tissue and tumor biopsy samples. *Sci Rep* 9(1):4836.

Figure 1

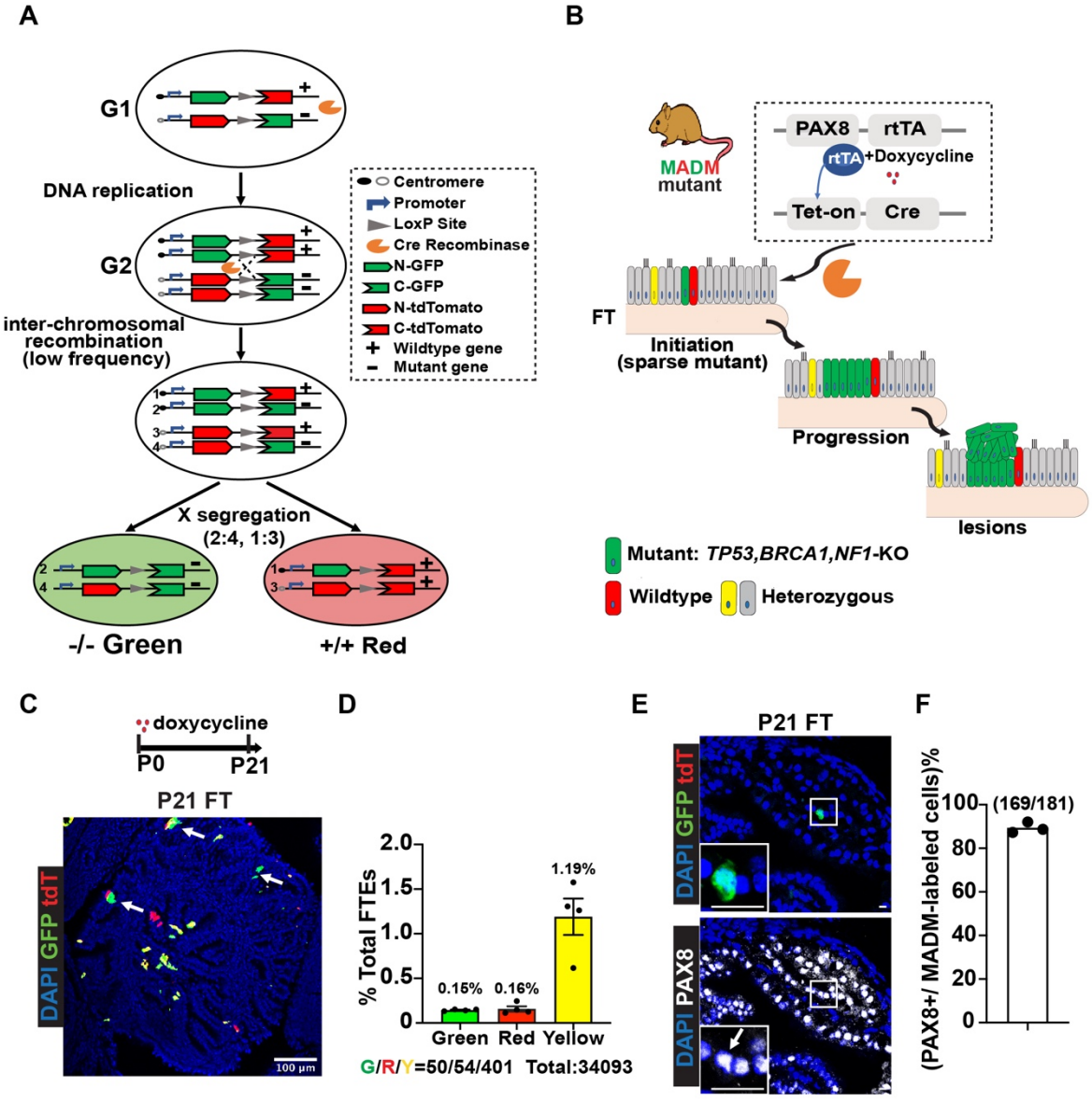
A
G1
DNA replication
G2
inter-chromosomal recombination (low frequency)
X segregation (2:4, 1:3)
-/- Green
+/+ Red
Centromere
Promoter
LoxP Site
Cre Recombinase
N-GFP
C-GFP
N-tdTomato
C-tdTomato
Wildtype gene
Mutant gene
B
MADM mutant
PAX8
rtTA
rtTA+Doxycycline
Tet-on
Cre
FT
Initiation (sparse mutant)
Progression
lesions
Mutant: TP53,BRCA1,NF1-KO
Wildtype
Heterozygous
C
doxycycline
P0
P21
P21 FT
DAPI GFP tdT
100 µm
D
% Total FTEs
0.15%
0.16%
1.19%
Green Red Yellow
G/R/Y=50/54/401 Total:34093
E
P21 FT
DAPI GFP tdT
DAPI PAX8
F
(PAX8+/ MADM-labeled cells)%
(169/181)

Figure 1. Establishment of a MADM-based mouse model for clonal tracing of initiated FT cells.

(A) MADM mechanism: MADM contains a pair of knock-in cassettes of chimeric GFP and tdTomato coding sequences, separated by a loxP-containing intron. Cre-mediated inter-chromosomal recombination in mitotic cells followed by X segregation generates singly colored cells with altered genotype. GFP expressing (Green) cells are homozygous mutant; tdTomato expressing (Red) cells are wildtype.

(B) The scheme of MADM-based modeling of HGSOC initiation in the FT.

(C) MADM labeled cells in FT after inducing Cre between post-natal day 0 and day 21 (P0-21).

(D) Percentage of green, red, and yellow cells among all FT epithelial cells (±SEM, *n*=3).

(E) MADM-labeled cells were positive for Pax8. Scale bar=50μm.

(F) Quantification of Pax8+% among all MADM-labeled cells. (*n* =3).

Figure 2

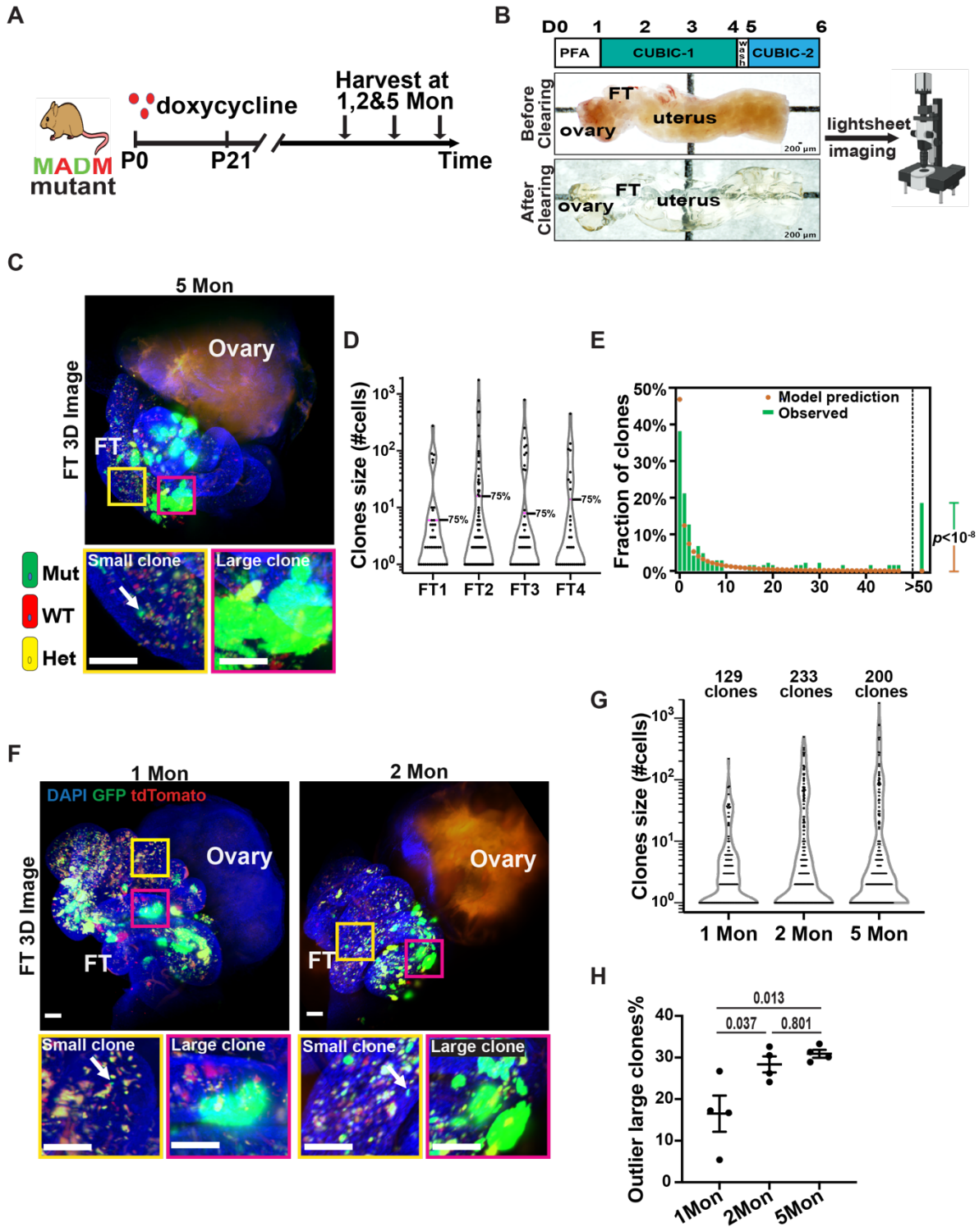
A
MADM mutant
doxycycline
P0
P21
Harvest at 1,2&5 Mon
Time
B
D0 1 2 3 4 5 6
PFA
CUBIC-1
CUBIC-2
Before Clearing
After Clearing
FT
ovary
uterus
200 µm
lightsheet imaging
C
5 Mon
FT 3D Image
Ovary
FT
Mut
WT
Het
Small clone
Large clone
D
Clones size (#cells)
75%
FT1
FT2
FT3
FT4
E
Fraction of clones
Model prediction
Observed
p<10-8
>50
F
1 Mon
2 Mon
DAPI GFP tdTomato
FT 3D Image
Ovary
FT
Small clone
Large clone
G
129 clones
233 clones
200 clones
Clones size (#cells)
1 Mon
2 Mon
5 Mon
H
Outlier large clones%
0.013
0.037
0.801
1Mon
2Mon
5Mon

Figure 2. Quantitative clonal tracing revealed divergent expansion of initiated cells.

(A) The scheme of DOX treatment and FT harvesting for measuring mutant clone size.

(B) The pipeline for high-resolution whole-FT imaging: fixed reproductive tracts were cleared though the CUBIC method and then 3D imaged with light-sheet microscopy.

(C) Representative 3D light-sheet images of cleared whole FT from 5-month old MADM-mutant mice (*n*=4). The yellow box shows non-expanded clones; the magenta box shows expanded clones. Scale bar=50 μm.

(D) Violin plot of clonal size distribution of mutant clones in four independent FTs from mice at 5 months of age.

(E) Fit of the observed clonal size distribution of mutant clones at 5 months to a negative binomial model. Bars show observed data; points show model prediction. Number of clones >50 cells observed is significantly higher than predicted. Fisher Exact Test, $p < 10^{-8}$.

(F) Representative 3D light-sheet images of cleared whole FT from 1- and 2-month old MADM-mutant mice (*n*=4). The yellow box shows non-expanded clones; the magenta box shows expanded clones. Scale bar=50 μm.

(G) Violin plot of clonal size distribution of mutant clones at 1 and 2 months. Data pooled from 4 mice.

(H) The portion of profoundly-expanded outlier clones detected at 1, 2, and 5 months. (± SEM, *n* = 4, Anova test with Tukey HSD)

Figure 3

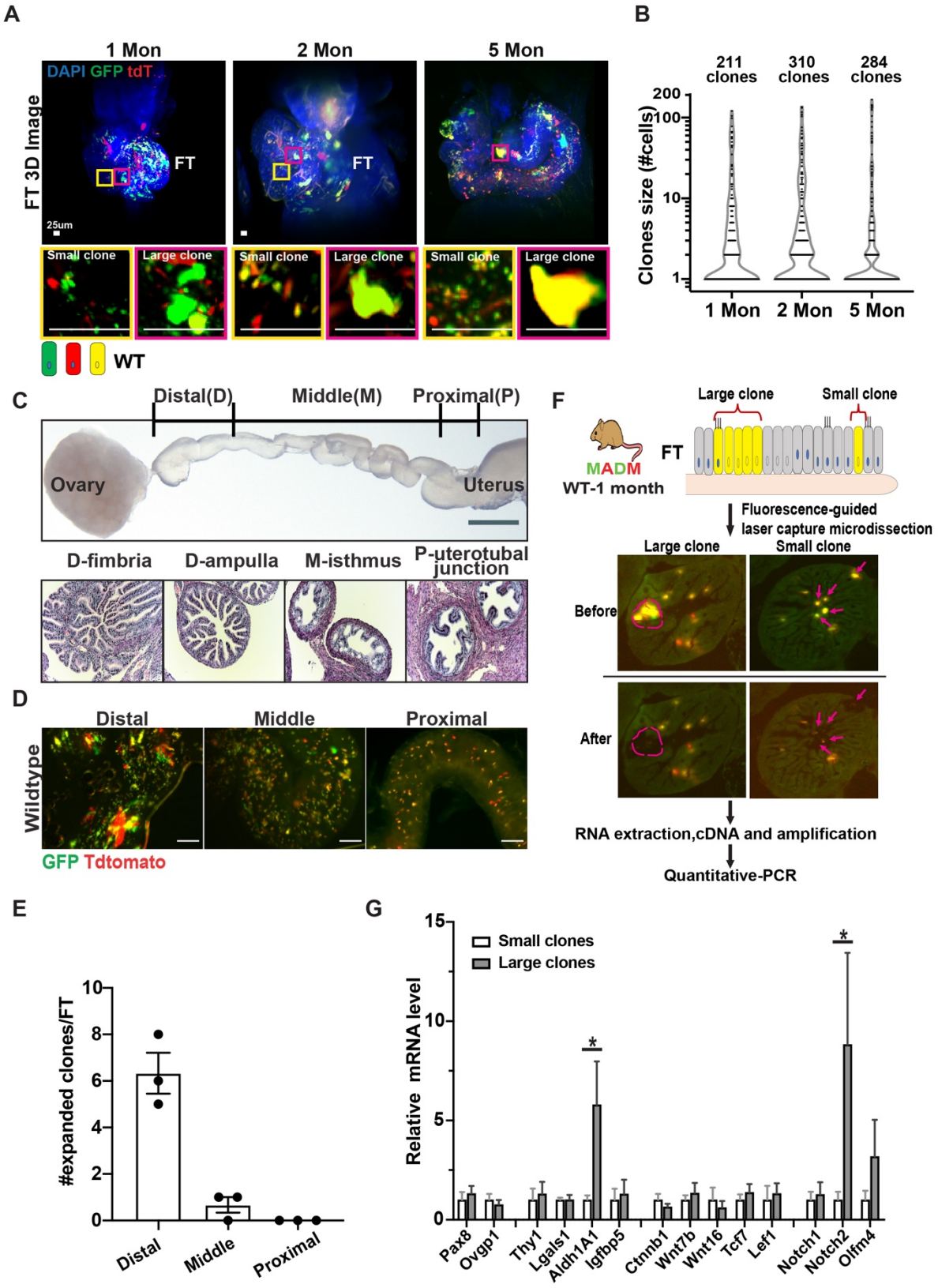
A
1 Mon
2 Mon
5 Mon
DAPI GFP tdT
FT 3D Image
FT
25um
Small clone
Large clone
WT
B
211 clones
310 clones
284 clones
Clones size (#cells)
200
100
10
1
1 Mon
2 Mon
5 Mon
C
Distal(D)
Middle(M)
Proximal(P)
Ovary
Uterus
D-fimbria
D-ampulla
M-isthmus
P-uterotubal junction
D
Distal
Middle
Proximal
Wildtype
GFP Tdtomato
E
#expanded clones/FT
10
8
6
4
2
0
Distal
Middle
Proximal
F
Large clone
Small clone
MADM
WT-1 month
FT
Fluorescence-guided laser capture microdissection
Large clone
Small clone
Before
After
RNA extraction,cDNA and amplification
Quantitative-PCR
G
Small clones
Large clones
Relative mRNA level
15
10
5
0
*
*
Pax8
Ovgp1
Thy1
Lgals1
Aldh1A1
Igfbp5
Ctnnb1
Wnt7b
Wnt16
Tcf7
Lef1
Notch1
Notch2
Olfm4

Figure 3. Spatial and molecular characterizations of expanded clones hint at a stem/progenitor-origin.

(A) Representative 3D light-sheet images of cleared whole FT from 1-, 2-, and 5-month old MADM-wildtype mice (*n*=3). The yellow box shows small clones; the magenta box shows expanded clones. Scale bar=25μm.

(B) Violin plot of clonal size distribution of wildtype clones at 1, 2, and 5 months. Data pooled from 3 mice.

(C) Upper panel: Whole-mount white-field image of a stretched FT from a two-month old MADM-wildtype mice, which can be separated into three portions based on distance to uterus. Lower panel: each FT region has distinct tubal morphology and inner folds shape. Scale bar= 500μm.

(D) Whole-mount fluorescence image of each segment of the stretched FT from MADM wildtype mice. Scale bar= 500μm.

(E) The number of expanded clones in distal (D), middle (M), and proximal (P) segments of FTs from 2-month old MADM-wildtype mice. (±SEM, *n*=3).

(F) The scheme of fluorescence-guided laser-capture microdissection of small and large clones from 1-month old MADM-wildtype mice (*n*=6), and cDNA library preparation for qRT-PCR.

(G) qRT-PCR analysis of expression of selected genes between small clones and large clones. ±SEM. Mann-Whitney U-test, *<0.05.

Figure 4

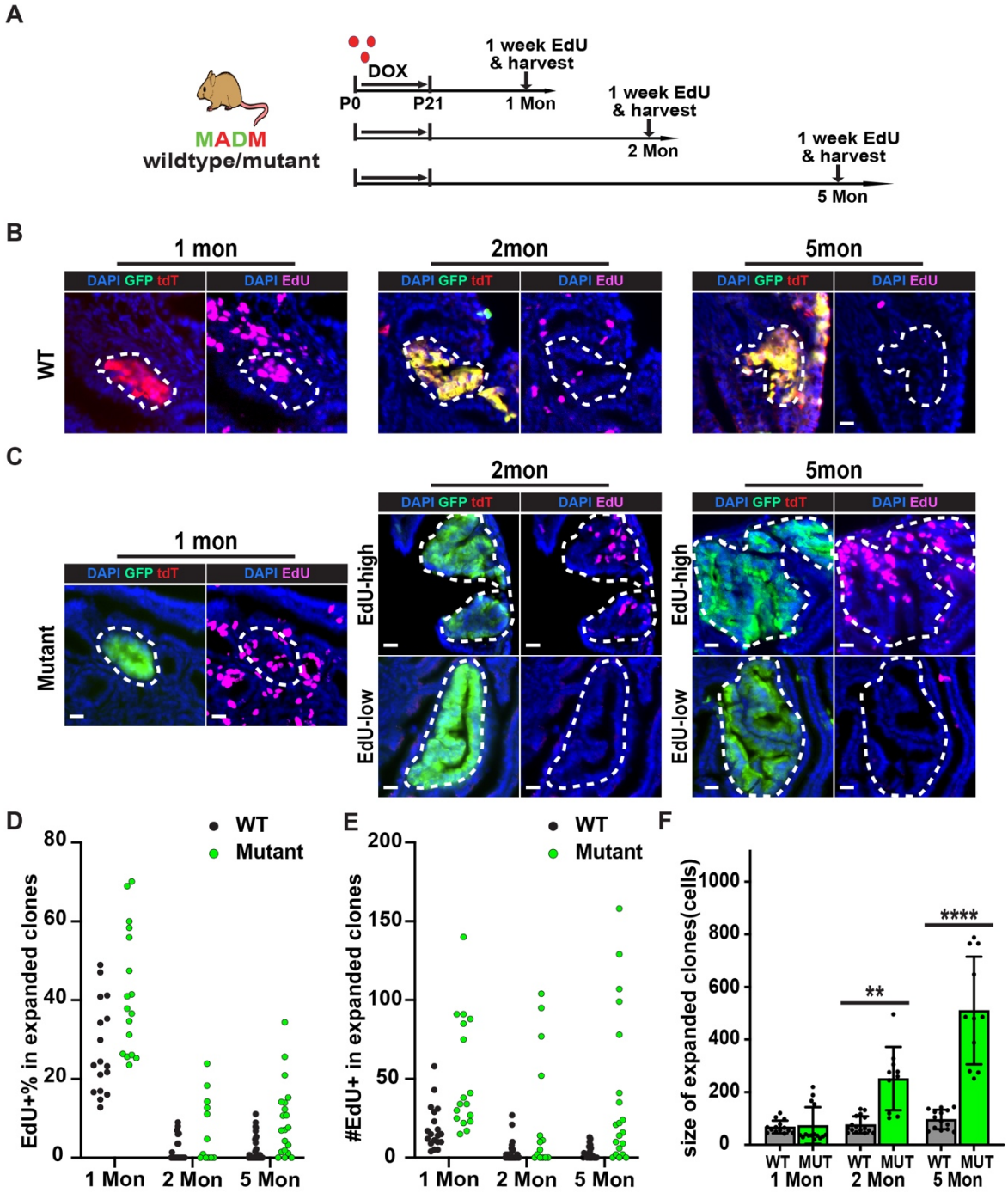
A
MADM
wildtype/mutant
DOX
P0
P21
1 week EdU & harvest
1 Mon
2 Mon
5 Mon
B
1 mon
2mon
5mon
DAPI GFP tdT
DAPI EdU
WT
C
Mutant
EdU-high
EdU-low
D
EdU+% in expanded clones
WT
Mutant
1 Mon
2 Mon
5 Mon
E
#EdU+ in expanded clones
F
size of expanded clones(cells)
WT
MUT
**
****

Figure 4. Oncomutations synergize with cell-intrinsic potential for sustained expansion of mutant clones.

(A) Scheme for EdU labeling and assessment of cell division in expanded wildtype and mutant clones over time.

(B) Representative images of EdU labeling in expanded wildtype clones at 1, 2, and 5 months. Scale bar=20μm.

(C) Representative images of EdU labeling in expanded mutant clones at 1, 2, and 5 months. Scale bar=20μm.

(D) EdU+% in each individual expanded wildtype and mutant clone at 1, 2, and 5 months. Data pooled from three mice.

(E) Number of EdU+ cells in each individual expanded wildtype and mutant clone at 1, 2, and 5 months. Data pooled from three mice.

(F) The average size of expanded wildtype clones and mutant clones from 1-, 2-, and 5-month old mice. ±SEM. t-test, **<0.01****<0.0001.

Figure 5

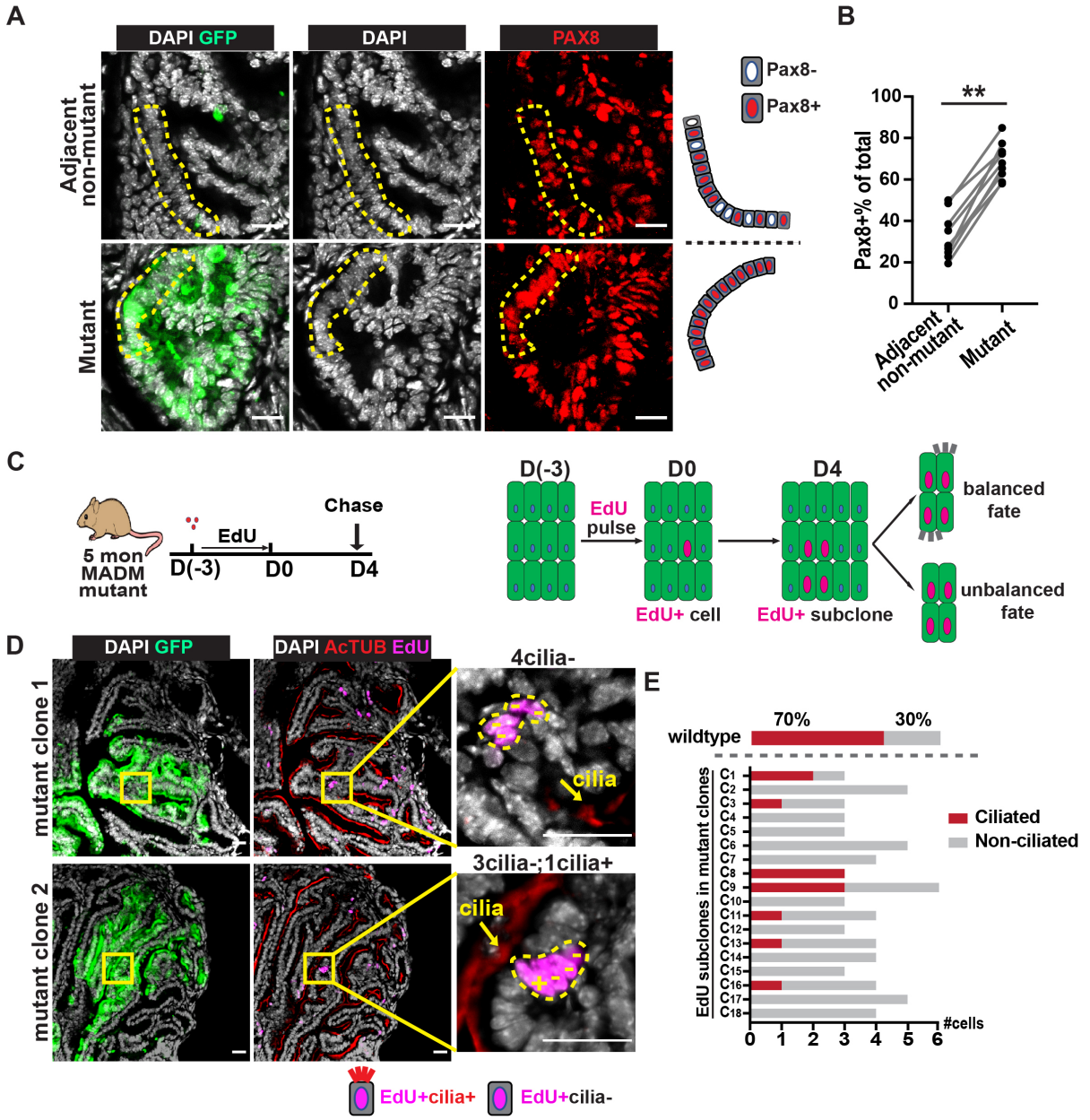

G

Age (month)	Total (*n*)	Fallopian tube	
		Normal	STIC
2	7	7	0
3	5	5	0
4	6	6	0
5	9	9	0
6	16	16	0
8	7	6	1
10	9	7	2
12	5	3	2
14	19	16*	1

Histopathological evaluation of FTs from MADM-mutant mice. * in two mice, FTs were engulfed by uterine tumor

Figure 5. Progressive mutant clones showed increase propensity to produce Pax8+ cells.

(A) Representative images of Pax8+ cell distribution in progressive mutant clones (lower panel) and in adjacent non-mutant regions (upper panel). The mutant clones showed continuous expansion of Pax8+ cells. Scale bar=20μm.

(B) The progressive mutant clones contained a higher portion of Pax8+ cells than adjacent non-mutant regions. Three mutant/non-mutant pairs were quantified from each of three mice in total. Wilcoxon-test, **<0.01.

(C) The scheme to perform clonal tracing of proliferating cells within progressive clones through EdU labeling and potential outcomes.

(D) Representative images show cellular composition of EdU subclones within progressive mutant clones. Upper panel shows a four-cell subclone with only non-ciliated cells. Lower panel shows a mixed subclone with one ciliated cell (+) and three non-ciliated cells (-). Scale bar=25μm.

(E) The cellular composition of EdU+ spots (>2 cells) within the mutant clones. In wildtype distal FT, ciliated cells account for the majority; however, in the EdU subclones within mutant clones, non-ciliated cells account for the majority.

(F) Immunofluorescence staining showing overlap of STICs with GFP, not tdTomato. Scale bar=50μm.

(G) STIC frequency in the FTs from MADM-mutant mice of an age cohort.

Figure S1

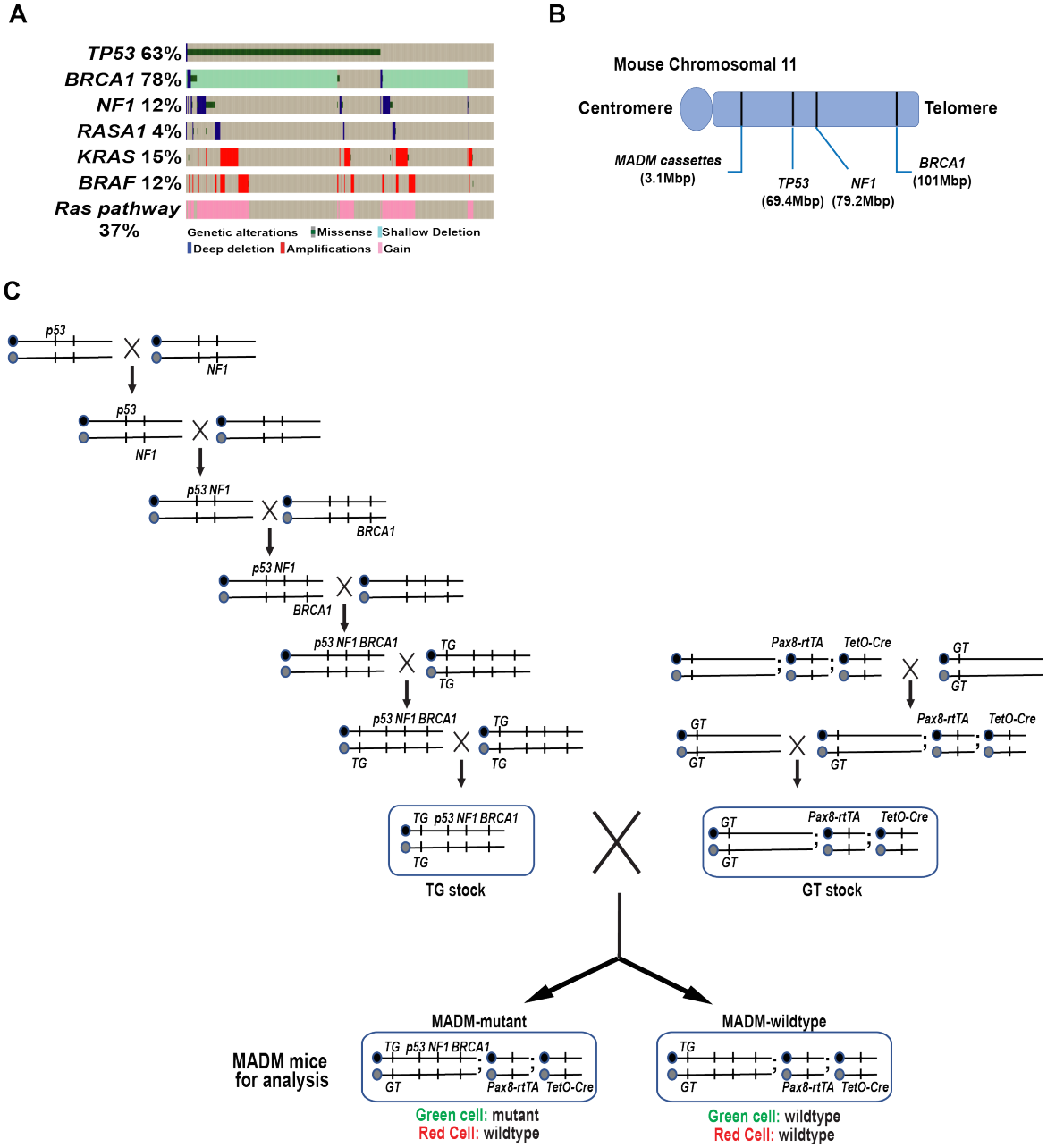
A
TP53 63%
BRCA1 78%
NF1 12%
RASA1 4%
KRAS 15%
BRAF 12%
Ras pathway 37%
Genetic alterations
Missense
Shallow Deletion
Deep deletion
Amplifications
Gain
B
Mouse Chromosomal 11
Centromere
Telomere
MADM cassettes (3.1Mbp)
TP53 (69.4Mbp)
NF1 (79.2Mbp)
BRCA1 (101Mbp)
C
p53
NF1
p53 NF1
BRCA1
p53 NF1 BRCA1
TG
Pax8-rtTA
TetO-Cre
GT
TG stock
GT stock
MADM-mutant
MADM-wildtype
MADM mice for analysis
Green cell: mutant
Red Cell: wildtype
Green cell: wildtype
Red Cell: wildtype

Figure S1. Additional details for initiating FT cells with MADM: mutation selection; chromosomal location of MADM cassettes and selected genes; and the breeding scheme to generate MADM-mutant and MADM-wildtype mice.

(A) Assessment of HGSOC mutation spectrum with TCGA datasets.

(B) The physical chromosomal locations of the MADM cassettes, TP53, BRCA1, and NF1 on mouse chromosome 11.

(C) The scheme to breed MADM-mutant mice and MADM-wildtype mice. We maintain two separate stocks and produce MADM mice through intercrossing the stocks. *TP53, BRCA1* and *NF1* mutations were incorporated into The TG stock, and the Cre transgenes (*Pax8-rtTA, TetO-Cre*) were incorporated into the GT stock.

Figure S2

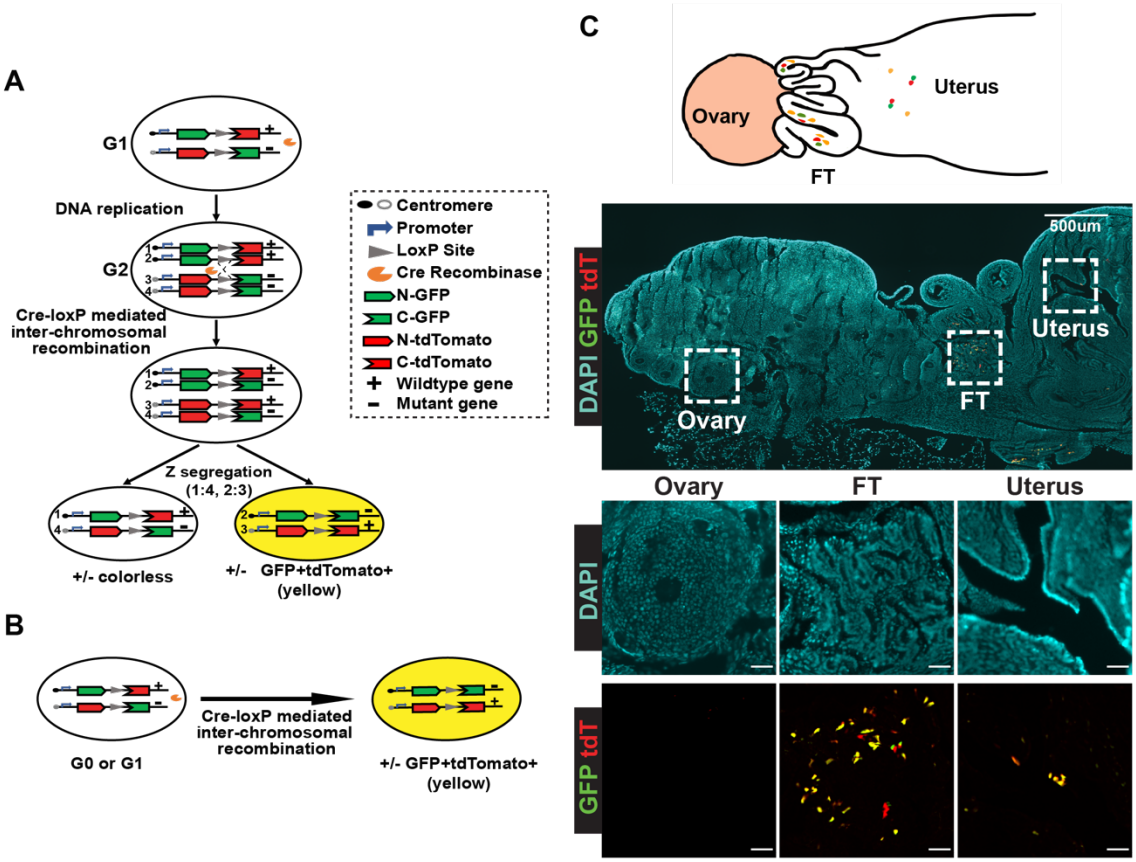
A
G1
DNA replication
G2
Cre-loxP mediated
inter-chromosomal
recombination
Z segregation
(1:4, 2:3)
+/- colorless
+/- GFP+tdTomato+
(yellow)
Centromere
Promoter
LoxP Site
Cre Recombinase
N-GFP
C-GFP
N-tdTomato
C-tdTomato
Wildtype gene
Mutant gene
B
G0 or G1
Cre-loxP mediated
inter-chromosomal
recombination
+/- GFP+tdTomato+
(yellow)
C
Ovary
Uterus
FT
DAPI GFP tdT
500um
Uterus
FT
Ovary
Ovary
FT
Uterus
DAPI
GFP tdT

Figure S2. Schematic mechanism of MADM to generate yellow cells without altering genotype, and MADM labeling specificity in the mouse reproductive tract.

(A) Cre-mediated inter-chromosomal mitotic recombination followed by Z segregation generates either colorless or double-colored yellow cells without altering the genotype.

(B) Cre-mediated inter-chromosomal recombination occurring in G1 or post-mitotic cells (G0) generates yellow cells without altering the genotype.

(C) MADM labeled cells are found in both the FT and the uterus but not in the ovary.

Figure S3

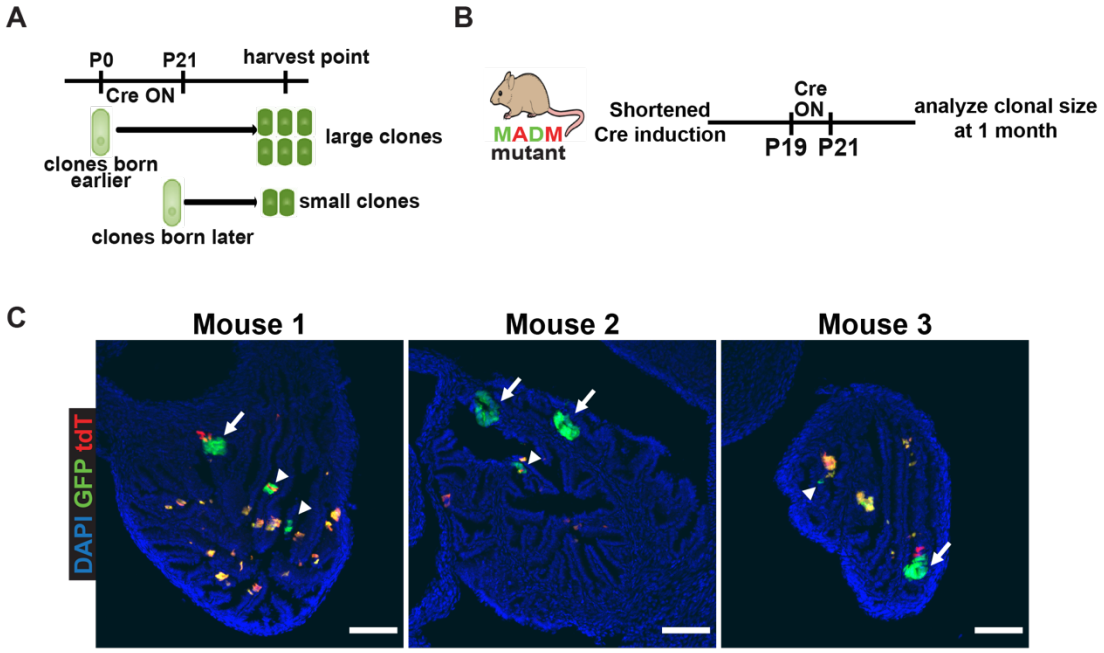
A
P0
P21
harvest point
Cre ON
clones born earlier
large clones
small clones
clones born later
B
MADM mutant
Shortened Cre induction
Cre ON
P19
P21
analyze clonal size at 1 month
C
Mouse 1
Mouse 2
Mouse 3
DAPI GFP tdT

Figure S3. Clonal size heterogeneity is not simply due to unsynchronized clonal age.

(A) The clonal age hypothesis: clones born earlier within the P0-21 range will show lager size at the harvest point, whereas clones born later will show smaller size.

(B) The scheme of DOX treatment to synchronize the clonal age of mutant cells.

(C) Representative images show heterogeneous size of MADM labeled clones in age synchronized mice (*n*=3). Arrows show expanded clones and arrowheads show non-expanded clones. Scale bar=100μm.

Figure S4

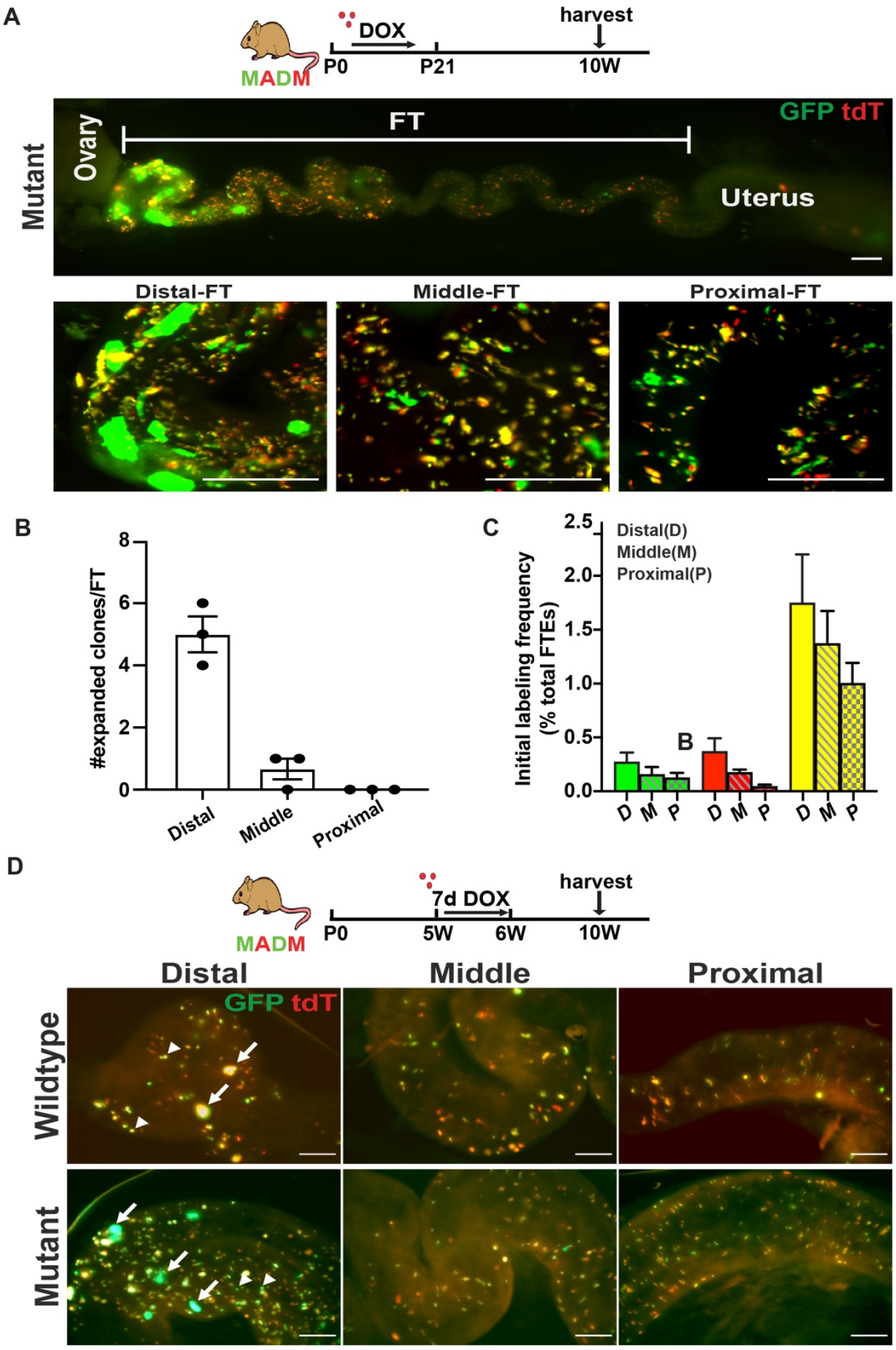
A
MADM
DOX
harvest
P0
P21
10W
Mutant
Ovary
FT
GFP tdT
Uterus
Distal-FT
Middle-FT
Proximal-FT
B
#expanded clones/FT
Distal
Middle
Proximal
C
Initial labeling frequency (% total FTEs)
Distal(D)
Middle(M)
Proximal(P)
D
7d DOX
5W
6W
Distal
Middle
Proximal
Wildtype
Mutant

Figure S4. Spatial distribution of expanded clones in MADM-mutant mice; MADM-labeling frequency in each FT segment initially; and spatial distribution of expanded clones when induced post-developmentally.

(A) Images of FT sections from 10-week old mutant FTs (*n*=3), showing that expanded mutant clones were mainly in the distal region. Scale bar=200μm.

(B) Quantification of the number of expanded clones in distal (D), middle (M), and proximal (P) regions from 10-week old MADM-mutant mice. (±SEM, *n*=3).

(C) Initial MADM labeling frequency in distal (D), middle (M), and proximal (P) FT regions immediately after P0-21 Doxycycline administration (*n*=3).

(D) Inducing MADM labeling in fully differentiated FTs: Doxycycline was administrated to MADM-wildtype/mutant mice between 5-6 weeks, then FTs were assessed at 10 weeks. Upper panel: wildtype FT; Lower panel: mutant FT. Expanded clones (arrows) and single cell clones (arrowheads) are shown. Scale bar=200μm.

Figure S5

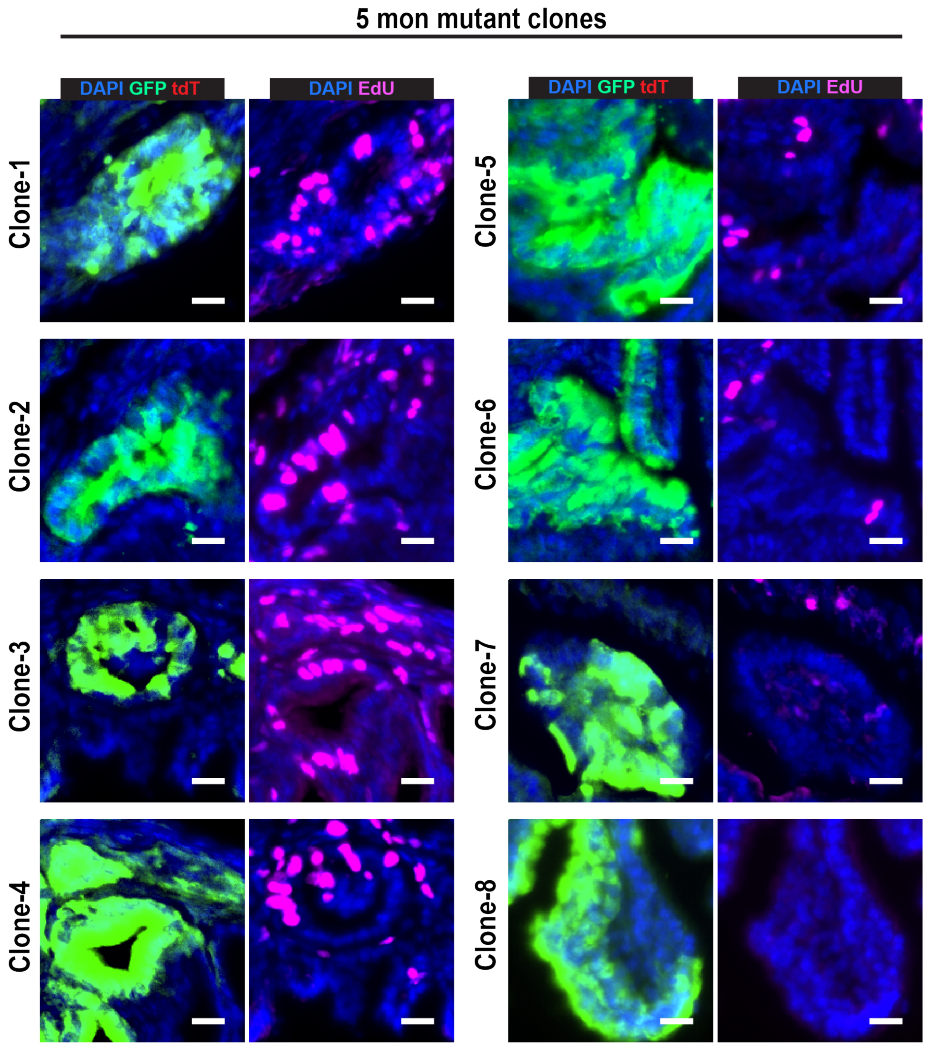
5 mon mutant clones
DAPI GFP tdT
DAPI EdU
DAPI GFP tdT
DAPI EdU
Clone-1
Clone-2
Clone-3
Clone-4
Clone-5
Clone-6
Clone-7
Clone-8

Figure S5. Additional images of EdU labeling in expanded mutant clones at 5 months of age. Clone-1, 2, 3, and 4 are highly proliferative, while clone-5, 6, 7, and 8 are relatively quiescent. Scale bar=20μm.

Figure S6

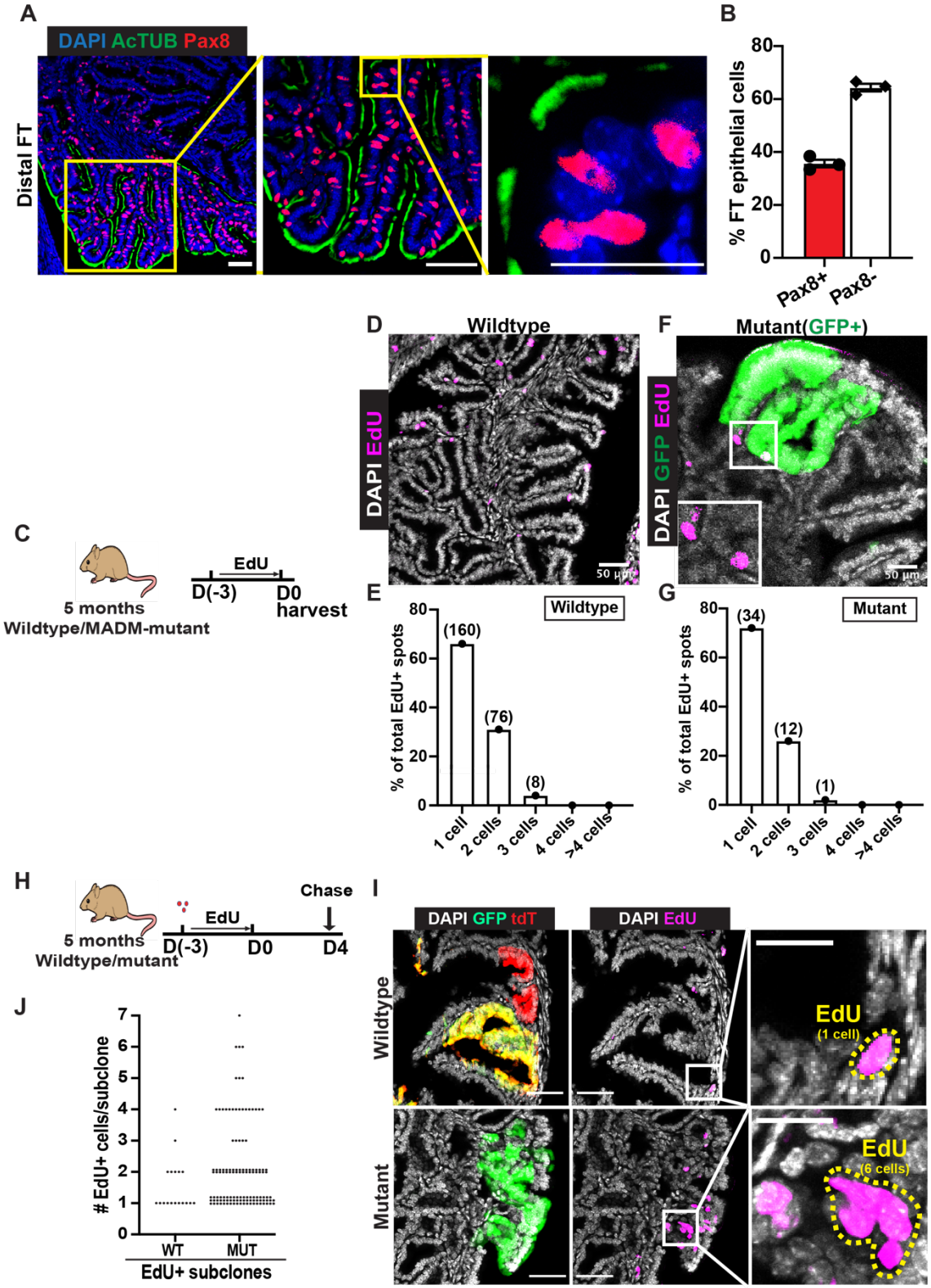
A
DAPI AcTUB Pax8
Distal FT
B
% FT epithelial cells
80
60
40
20
0
Pax8+
Pax8-
C
5 months
Wildtype/MADM-mutant
EdU
D(-3)
D0
harvest
D
Wildtype
DAPI EdU
50 µm
F
Mutant(GFP+)
DAPI GFP EdU
50 µm
E
Wildtype
% of total EdU+ spots
(160)
(76)
(8)
1 cell
2 cells
3 cells
4 cells
>4 cells
G
Mutant
(34)
(12)
(1)
H
5 months
Wildtype/mutant
EdU
Chase
D(-3)
D0
D4
I
DAPI GFP tdT
DAPI EdU
Wildtype
Mutant
EdU
(1 cell)
EdU
(6 cells)
J
EdU+ cells/subclone
WT
MUT
EdU+ subclones

Figure S6. The Pax8+ cell distribution pattern in wildtype distal FT, and 3-day EdU labeling marked cells at clonal density.

(A) Alternating Pax8+ and AcTUB+ cells in the distal FT from 5-month wildtype mice. Scale bar=50μm for left and middle panels, scale bar=25 μm for right panel.

(B) Percentage of Pax8+ and Pax8- cells in the distal FT. (±SEM, *n*=3).

(C) Scheme for EdU treatment and analysis.

(D) EdU staining in wildtype FTs revealed that EdU-labeled cells were scattered and most EdU+ spots consist of one cell or two cells. Scale bar=50μm. Representative image from 3 mice.

(E) The size distribution of EdU+ spots in FTs from 5-month old wildtype mice (*n*=3). The total number of EdU spots (n) is shown above the bar graph.

(F) EdU staining in mutant FTs revealed that EdU-labeled cells were also scattered, and most EdU+ spots are still shown one cell or two cells. Scale bar=50μm. Representative image from 3 mice.

(G) The size distribution of all EdU+ spots in FTs from 5-month MADM-mutant mice (*n*=3). The total number of EdU spots (n) is shown above the bar graph.

(H) Scheme for EdU pulse-chase assay.

(I) Upper panel: EdU clone of one cell within expanded wildtype clones when chased at day4. Lower panel: EdU clone of six cells within progressive mutant clones. Scale bar=20μm.

(J) The size of each EdU clone within expanded wildtype clones and progressive mutant clones. Data pooled from three mice for each group.

Figure S7

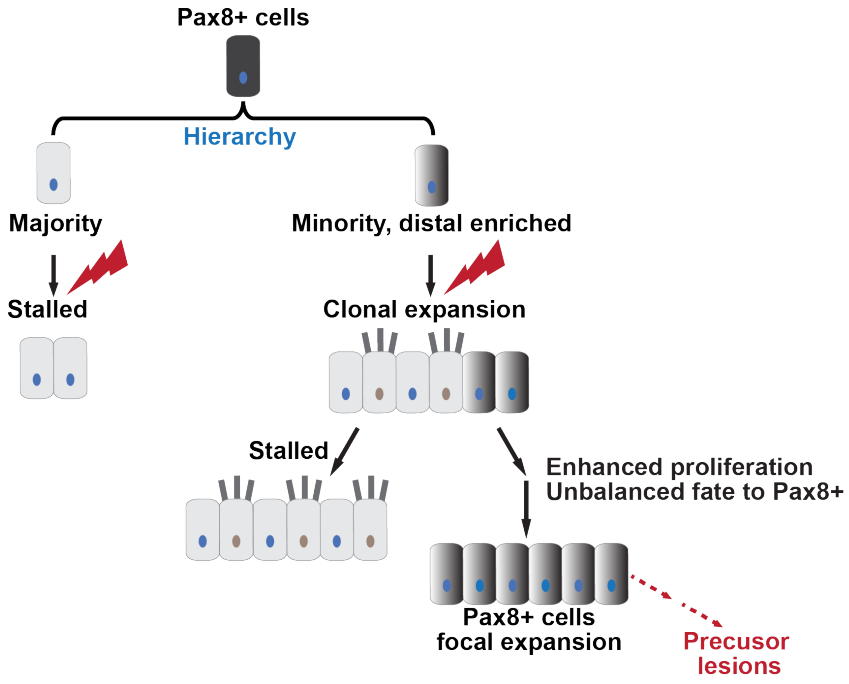

Figure S7. Schematic illustration of heterogeneous clonal dynamics of ovarian cancer-initiating cells in the fallopian tube

The initiated FT Pax8+ cells adopt distinct clonal expansion fate shortly after acquiring oncogenic mutations. While most of them stall quickly, a few distal mutant clones expand significantly. Among initially expanded mutant clones, many stall shortly after while some continue to progress. Elevated proliferation and imbalanced differentiation toward Pax8 fate of continuously progressing clones eventually leads the formation of precursor lesions known as STICs.